Check for updates

NMR in Biomedicine

WILEY

NMR IN BIOMEDICINE

RESEARCH ARTICLE OPEN ACCESS

In Vivo Imaging With a Low-Cost MRI Scanner and Cloud Data Processing in Low-Resource Settings

Teresa Guallart-Naval[1] | Robert Asiimwe[2] | Patricia Tusiime[2] | Mary A. Nassejje[2] | Leo Kinyera[2] | Lemi Robin[2] | Maureen Nayebare[2,3] | Luiz G. C. Santos[1] | Marina Fernández-García[1] | Lucas Swistunow[1] | José M. Algarín[1] | John Stairs[4] | Michael Hansen[4] | Ronald Amodoi[2] | Andrew Webb[5] | Joshua Harper[6,7] | Steven J. Schiff[8] | Johnes Obungoloch[2] | Joseba Alonso[1]

[1]MRILab, Institute for Molecular Imaging and Instrumentation (i3M), Consejo Superior de Investigaciones Científicas (CSIC) & Universitat Politècnica de València (UPV), Valencia, Spain | [2]Department of Biomedical Engineering, Mbarara University of Science and Technology (MUST), Mbarara, Uganda | [3]Department of Radiology, Leiden University Medical Center (LUMC), Leiden, the Netherlands | [4]Facultad de Ciencias Aplicadas, Universidad Comunera, Asuncion, Paraguay | [5]Microsoft Research, Health Futures, Redmond, Washington, USA | [6]Department of Neurosurgery, Yale University, New Haven, Connecticut, USA | [7]Department of Epidemiology of Microbial Diseases, Yale University, New Haven, Connecticut, USA | [8]Department of Biological and Biomedical Engineering, McGill University, Montreal, Canada

Correspondence: Joseba Alonso (joseba.alonso@i3m.upv.es)

Received: 26 November 2025 | **Revised:** 25 March 2026 | **Accepted:** 30 March 2026

ABSTRACT

The goal of this work is to demonstrate in vivo imaging with a low-cost, low-field MRI scanner built and operated in Africa and to show how systematic hardware and software improvements can mitigate the main operational limitations encountered in low-resource environments. To this end, a 46-mT Halbach scanner located at the Mbarara University of Science and Technology (Uganda) was upgraded through a complete reorganization of grounding and shielding, installation of new control electronics, and open-source user-interface software. Noise performance was quantified using a standardized protocol and in vivo brain images were acquired with three-dimensional RARE sequences. Distortion correction was implemented using cloud-based reconstructions incorporating magnetic field maps. The revamped system reached noise levels routinely below three times the thermal limit and demonstrated stable operation over multi-day measurements. Three-dimensional T_1- and T_2-weighted brain images were successfully acquired and distortion-corrected with remote GPU-based reconstructions and near real-time visualization through the user interface. The results show that low-cost MRI systems can achieve clinically relevant image quality when electromagnetic noise and power-grid instabilities are properly addressed. This work highlights the feasibility of sustainable MRI development in low-resource settings and identifies stable power delivery and local capacity building as the key next steps toward clinical translation.

1 | Introduction

The lack of access to essential radiological infrastructure compromises the quality of healthcare services and signifies a prominent burden on low and middle income countries (LMICs). Specifically, present-day magnetic resonance imaging (MRI) technologies remain out of reach for about 70% of the world population [1, 2], despite estimates that millions of lives could be saved every year by making it more widely available [3].

The MRI accessibility problem takes different shapes in different regions [1, 2]. In sub-Saharan Africa (SSA), formed by 54 countries and with a total population of over 1.2 billion people [4], a recent needs assessment survey identified brain, spine, and musculoskeletal imaging applications as most relevant [5]. This is motivated by a number of factors. One is that SSA accounts for roughly half of the global incidence of hydrocephalus cases (90% of the cases appear in LMICs, mostly in pediatric populations) [6]. While ultrasound and CT are commonly

This is an open access article under the terms of the Creative Commons Attribution-NonCommercial License, which permits use, distribution and reproduction in any medium, provided the original work is properly cited and is not used for commercial purposes.

© 2026 The Author(s). *NMR in Biomedicine* published by John Wiley & Sons Ltd.

used for initial diagnosis, MRI plays a key role in non-ionizing assessment, surgical planning, and post-shunting monitoring [7]. Another is that the burden of non-communicable diseases in Africa steadily increases as environmental and societal trends evolve. For instance, stroke is now more prevalent in the African continent than in Western Europe and the United States [5], and MRI is the recommended standard of care for these (and multiple other) neurological diseases [8]. Spine and musculoskeletal applications are motivated mostly by traffic accidents. For reference, traffic deaths on African roads add up to about one quarter of the victims worldwide, while possessing barely 2% of the world's vehicle fleet [9, 10]. Likewise, the incidence of non-fatal accidents is extreme in SSA, and MRI could play a key role for traumatic spine [11] and extremity injuries [12, 13].

However, MRI machines are complex, proprietary, and extraordinarily expensive. Furthermore, they necessitate highly-trained staff for their operation. These aspects, combined with the scarce economic, material, and trained human resources available, preclude the penetration of present-day MRI in SSA and other LMICs. Low-field MRI technologies (LF-MRI) operate below 0.5 T, use permanent rather than superconducting magnets, and have been postulated as a means to alleviate this situation [7, 8, 14–18]. Relevant milestones achieved with LF-MRI systems include point-of-care imaging [19–25], home healthcare [26], quantitative MRI and fingerprinting [27, 28], hard-tissue imaging [29–31], artifact-free imaging of metallic implants [26, 32], robust 3D and diffusion imaging at low field [33], or whole-body imaging [34]. Still, as of today, translation to the clinic of most of the prospective LF-MRI applications remains to be demonstrated, more so for deployment in low-resource settings, where there are multiple operational challenges other than the system cost (see Section 2).

In this paper, we present in vivo images taken with a low-cost ($\sim$ 30 k$) LF-MRI system built in Africa. The 46-mT Halbach scanner had already been constructed on site at the Mbarara University of Science and Technology (MUST), in Uganda [35]. To make it suitable for in vivo imaging, we have revised the complete electronics setup and installed the latest stable versions of the control electronics and user interface applications (MaRCoS and MaRGE, [36, 37]). Additionally, we have upgraded MaRCoS to integrate with Tyger, an open-source framework for remote signal processing [38]. As part of this work, the MUST team has gathered and documented know-how and methodologies followed in the laboratories of the Institute for Molecular Imaging and Instrumentation (i3M, Valencia, Spain) and the Leiden University Medical Center (LUMC, Leiden, The Netherlands), thereby increasing the local expertise and autonomy.

2 | System Baseline and Challenges

2.1 | System Baseline

The MRI scanner at MUST [35] is built around a 46-mT permanent magnet array in a Halbach configuration, without any passive shimming. Over a 20-cm diameter spherical volume, the resulting B_0 inhomogeneity is approximately 4700 ppm. The magnet weighs $<$ 100 kg and is mounted on an aluminum trolley with supports for the gradient and radio-frequency (RF) subsystems. The gradient set was manufactured in Uganda from copper wire wound onto 3D-printed formers, following designs supplied by the collaborating institutions. The gradient power amplifier (GPA) follows an open-source design that provides up to $\pm$ 15 A and $\pm$ 10 V [39]. The RF chain consisted of a single solenoidal coil connected to a non-gated, commercial low-noise amplifier (LNA) and a home-made unblanked transmit/receive (TxRx) switch. Power amplification for the gradients relied on an open-source design [39] and RF transmission made use of a commercial 1-W power amplifier (RFPA). The scanner was controlled using an early version of the open-source MaRCoS platform. At the time, the software did not include the MaRGE graphical interface, and all operation was handled via low-level scripts and command-line tools.

This installation at MUST in 2023 represented the first documented on-site construction of an MRI system in SSA, enabling basic imaging (Figure 1a,b) and marking an important proof of concept that demonstrated the feasibility of LF-MRI in a resource-limited environment.

While the system produced images, its operation revealed important limitations for progression toward in vivo imaging. Most prominently, the early images suffered from low signal-to-noise ratio (SNR) and geometric distortions, falling short of the robustness and usability required for clinical translation. For reference, the bell pepper image in Figure 1 took hours to acquire.

2.2 | Challenges

Here, we summarize the operational challenges encountered for in vivo imaging with the 2023 setup, providing the baseline against which the hardware and software upgrades presented later in the paper should be interpreted.

2.2.1 | Electromagnetic Noise and Power Grid Reliability

Operation at low magnetic field strengths is intrinsically challenging because the induced NMR signals are weak and image quality is ultimately limited by the signal-to-noise ratio (SNR) [40]. In the baseline MUST system, this problem was exacerbated by the absence of any RF shielding around the magnet and, more importantly, by suboptimal grounding of the system, which left the receive chain highly exposed to radiated electromagnetic interference (EMI). As a result, the effective noise floor was sizable and fluctuated strongly even between consecutive acquisitions.

The impact of the electromagnetic environment is illustrated in Figures 2a,b, which show noise levels logged over a few hours. Even with the later, optimized version of the scanner, the measurements reveal a clear dependence on electrical activity within the building and on the state of the local power grid, if grounding is suboptimal.

On top of this already noisy environment, the reliability of the grid itself represents an additional limitation. In Mbarara,

10991492, 2026, 6, Downloaded from https://analyticalsciencejournals.onlinelibrary.wiley.com/doi/10.1002/nbm.70293 by Mbarara Univ of Science and Tec, Wiley Online Library on [13/05/2026]. See the Terms and Conditions (https://onlinelibrary.wiley.com/terms-and-conditions) on Wiley Online Library for rules of use; OA articles are governed by the applicable Creative Commons License



FIGURE 1 | System evolution at MUST. (a) Scanner after the initial assembly in 2023. (b) First reconstructed image (bell pepper). Front (c), rear (d), and global (e) views of the MUST scanner in the present configuration, highlighting the improved electronics setup, RF coils, and mechanical integration. (f) MaRGE user interface.

extended outages and short blackouts are frequent, forcing scanner downtime and occasionally corrupting acquisitions, despite the diesel generator available in campus. Figure 2c summarizes the power interruptions recorded over a two-week period, underscoring the need for autonomous and stable power solutions.

2.2.2 | Access to Material and Computational Resources

Carrying out MRI research and system development in low-resource settings is inevitably constrained by the limited availability of technical components and laboratory infrastructure. In the case of the MUST scanner, access to basic electronic parts such

10991492, 2026, 6, Downloaded from https://analyticalsciencejournals.onlinelibrary.wiley.com/doi/10.1002/nbm.70293 by Mbarara Univ of Science and Tec, Wiley Online Library on [13/05/2026]. See the Terms and Conditions (https://onlinelibrary.wiley.com/terms-and-conditions) on Wiley Online Library for rules of use; OA articles are governed by the applicable Creative Commons License

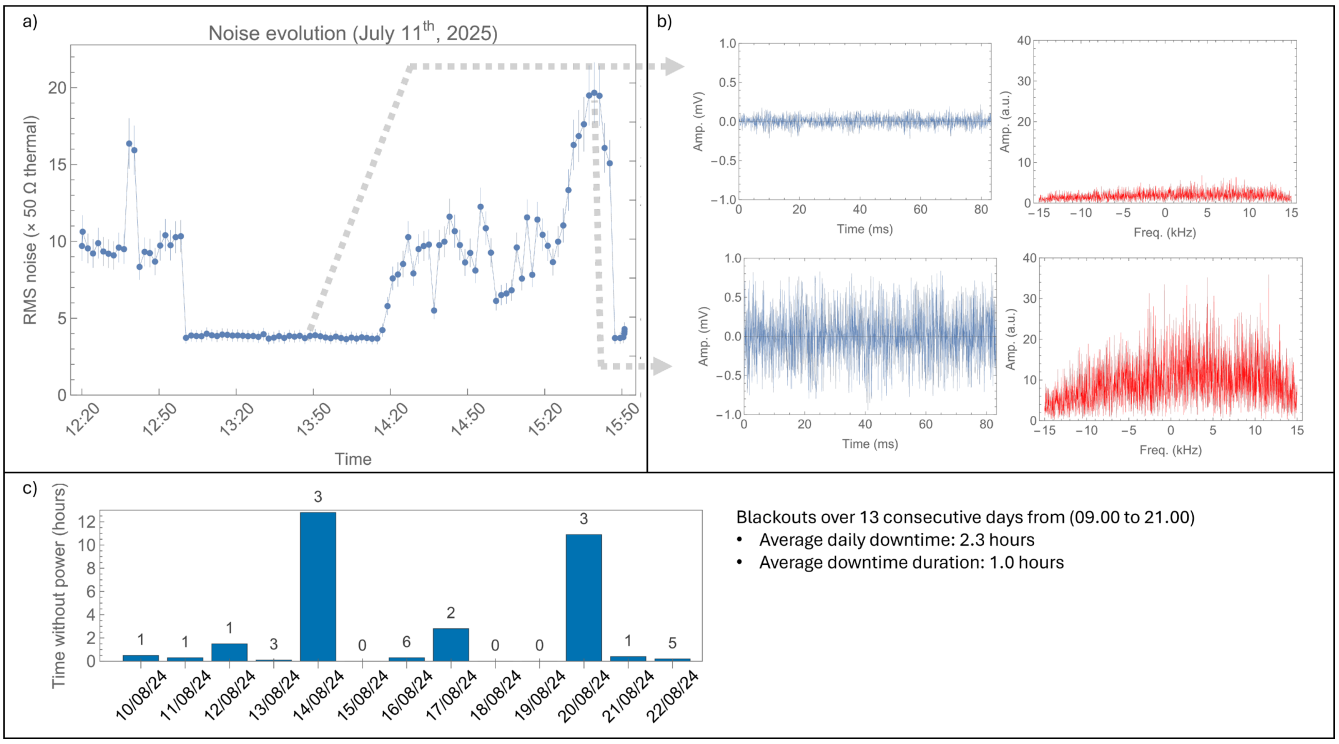


FIGURE 2 | Electromagnetic environment at MUST. (a) Noise levels logged over a few hours after the revamp but with suboptimal grounding, highlighting the strong dependence of the measured noise floor on building activity and grid conditions. (b) Inserts show representative traces and spectra under "quiet" and "noisy" conditions. (c) Frequency of power-off events recorded over a 2-week period.

as connectors, coaxial cables, or measurement instruments is limited, often requiring long procurement times or international shipping. These limitations compound the effects of electromagnetic interference discussed above, since effective noise suppression and shielding depend critically on appropriate materials and hardware.

In this regard, illustrative examples encountered during this work include: (i) the fact that the system operates with a 1-W RF power amplifier, whereas similar setups in partner laboratories employ units in the 250-W to 1-kW range; (ii) when one of the diodes in the passive TxRx switch failed, its replacement was delayed by the absence of local suppliers, and standard diodes that cost only a few cents elsewhere had to be substituted with a lower-grade alternative that was both more expensive and slow to obtain; (iii) precision mechanical work is also challenging and the lack of laser-cutting services in Mbarara limited the ability to fabricate accurate shimming inserts, hindering fine adjustment of the magnetic field homogeneity as routinely performed in comparable Halbach magnets [41].

Finally, computational resources present an additional bottleneck. High-end workstations and GPUs are not readily available, and subscription-based cloud services are often unaffordable. Even the control computer used to operate the MUST scanner offers modest performance, affecting data throughput and the ability to perform advanced reconstructions locally.

3 | Methods

The two main activities carried out in this work were the upgrade of the MUST scanner to achieve improved operational capabilities and the acquisition of in vivo images to demonstrate the impact of these improvements.

3.1 | Scanner Revamp and Electromagnetic Noise Suppression

The scanner revamp focused on four main aspects (Figure 1c–f): a complete overhaul of grounding and shielding; multiple new RF coils and impedance-matching electronics; the installation of the latest releases of MaRCoS and MaRGE; and the integration of Tyger for cloud-based data processing and image reconstruction.

A comprehensive reorganization of the grounding and shielding layout was carried out following the guidelines detailed in Ref. [40]. Particular attention was paid to cable management, enclosure integrity, and the definition of a single, low-impedance ground reference for the entire system (Figure 3). All electronic subsystems were enclosed in conductive aluminum housings with robust electrical contact between panels and lids, ensuring continuous shielding and minimizing radiative leakage. Internal RF shielding around the receive coil was reinforced with a short, thick connection between the coil return and the inner copper sleeve, while the outer shield was bonded to all major enclosures and cable shields following, where possible, a star-grounding configuration. Gradient cables were rerouted and shielded to suppress inductive coupling, and all "noisy" elements (such as power supplies, digital control boards, and switching regulators) were relocated away from the RF path. Only linear power supplies were used for the analog subsystems, explicitly avoiding switch-mode supplies to reduce conducted and radiated EMI.

10991492, 2026, 6, Downloaded from https://analyticalsciencejournals.onlinelibrary.wiley.com/doi/10.1002/nbm.70293 by Mbarara Univ of Science and Tec, Wiley Online Library on [13/05/2026]. See the Terms and Conditions (https://onlinelibrary.wiley.com/terms-and-conditions) on Wiley Online Library for rules of use; OA articles are governed by the applicable Creative Commons License

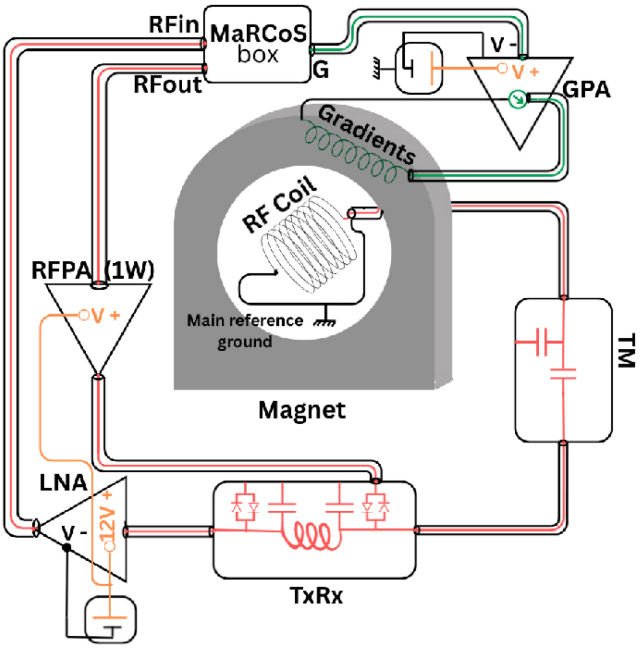


FIGURE 3 | Schematic of the complete electronics setup of the MUST scanner after the revamp. Red lines indicate RF signal paths (transmit and receive), green lines correspond to gradient drive signals, orange lines denote power connections, and black lines represent ground. The diagram highlights the main subsystems, including the magnet, RF and gradient coils, TxRx switch, LNA, 1-W RFPA, GPA, and the MaRCoS control unit.

In addition, any component containing a ferromagnetic core and directly driven at 50 Hz (such as the transformers inside linear supplies, or mains-driven electromechanical relays) was either removed or positioned at a sufficient distance from the magnet. These elements generate alternating magnetic fields that modulate the Larmor frequency and introduce artifacts unless echo and repetition times are exact multiples of 20 ms. For acquisition windows exceeding a few ms, such modulation can also distort the readout signal, as the field may vary significantly within that interval. Both effects become apparent already for sub-nano-tesla modulation depths. While increasing the distance from the magnet effectively mitigates B_0 modulation, it also necessitates longer cable runs, which in turn raise susceptibility to noise pickup and ground potential differences.

As part of the hardware upgrade, several new RF coils were constructed to replace the single cylindrical solenoid used in the original setup (Figure 1c,d). The primary head coil consists of a single-layer spiral geometry adapted to the head anatomy, following the design described in Ref. [16]. This provides an improved filling factor and enhanced SNR for brain imaging. In addition, two solenoidal coils were built: one optimized for head imaging and another, smaller version for, for example, knee acquisitions.[1] A new impedance tuning and matching (TM) box was also developed, incorporating multiple capacitors on rotary switches that allow manual selection among discrete capacitance values without the need for soldering.[2]

The control and user interface software were upgraded to the latest stable releases of MaRCoS [43] and MaRGE [37, 44]. The new MaRGE version provides a unified graphical environment programmed in Python, integrating pulse sequence control, system calibration, and reconstruction tools within a modular layout. It replaces the early command-line interface used in the original system, offering enhanced usability, real-time monitoring, and compatibility with standardized sequence formats such as Pulseq.

The system was also equipped with Tyger, an open-source platform that enables streaming of raw MR data from the scanner to cloud-based computational resources, where reconstructions or post-processing tasks can be executed inside Docker containers.[3]

Noise measurements were performed following the stepwise protocol described in Ref. [40], adapted here for the MUST system (Figure 4a) in an unshielded laboratory environment. At MHz-range Larmor frequencies, the fundamental noise limit is set by thermal (Johnson-Nyquist) noise from the receiver impedance. For a 50 Ω source at room temperature (≈ 300 K), connected to a 50 Ω input LNA, the theoretical voltage noise spectral density is $\approx 0.45\ \mathrm{nV}/\sqrt{\mathrm{Hz}}$, defining a baseline that corresponds to one "thermal unit." Measured RMS voltages were normalized to this reference. Each measurement used a 30-kHz bandwidth and lasted 80 ms, covering four full cycles of the 50-Hz mains to capture periodic interference components.

Noise characterization was carried out following a staged and incremental protocol designed to isolate the dominant noise contributions along the receive chain. As a reference, the expected thermal noise floor of the system was first estimated from the known characteristics of the receive electronics, providing a baseline against which all subsequent measurements were compared. Experimental measurements then began with a minimal receive configuration, consisting only of the LNA, ADC, and control electronics, with a 50 Ω terminator connected directly at the LNA input. This configuration allows verification that the intrinsic electronic noise of the receive chain is close to the theoretical limit and facilitates the identification of faulty components, grounding issues, or power-supply-related interference if excess noise is observed.

Starting from this baseline, additional subsystems were progressively integrated into the setup, including the Tx/Rx switch, transmit chain, RF power amplifier, gradient cabling, and gradient power amplifiers, with noise measurements repeated after each step. This incremental approach enables direct attribution of excess noise to specific hardware elements or electromagnetic coupling paths. After completion of this process, the 50 Ω load was replaced by the RF coil and its tuning and matching network, and the same staged measurements were repeated with the coil both unloaded and loaded by an in vivo subject. This final step captures the combined effects of coil sensitivity, external electromagnetic interference, and subject-induced loading, providing a realistic assessment of system noise under operational conditions. Importantly, the coil and in vivo measurements differed only in the absence/presence of the human subject; the physical setups were otherwise identical (patient table, conductive blanket, etc.) to that in Figure 1e.

Such noise measurements can be acquired with a dedicated sequence implemented in MaRGE, which opens the ADC for a

10991492, 2026, 6, Downloaded from https://analyticalsciencejournals.onlinelibrary.wiley.com/doi/10.1002/nbm.70293 by Mbarara Univ of Science and Te, Wiley Online Library on [13/05/2026]. See the Terms and Conditions (https://onlinelibrary.wiley.com/terms-and-conditions) on Wiley Online Library for rules of use; OA articles are governed by the applicable Creative Commons License

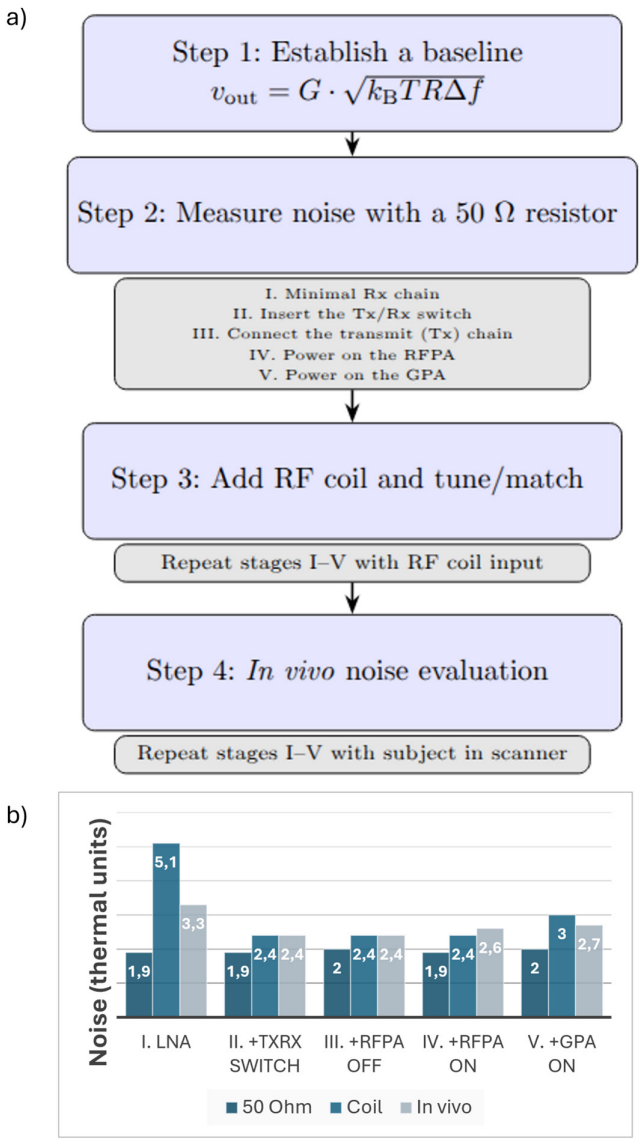


FIGURE 4 | Electromagnetic noise characterization and suppression in the MUST scanner. (a) Four-step protocol for systematic noise assessment in low-field MRI systems, adapted from Ref. [40]. Steps 2–4 involve repeated measurements through stages I–V to isolate the contribution of each subsystem as the scanner is progressively assembled and powered. The expression $v_{out} = G \cdot \sqrt{k_B T R \Delta f} = G \cdot v_n/2$ defines the expected baseline noise voltage, where G is the linear transducer gain of the amplifier, $k_B \approx 1.38e-23\ J/K$ is Boltzmann's constant, and v_n is the RMS voltage noise generated by a resistor R at temperature T over a bandwidth Δf. (b) Normalized noise measurements, expressed as multiples of the theoretical thermal limit, for the different hardware configurations in the protocol, with colored bars corresponding to Steps 2–4, and the labels in the abscissa to Stages I–V.

predefined acquisition window and returns the recorded signal for subsequent analysis. The resulting data reflect the internal signal pre-processing steps configured in the control system, including oversampling, decimation, and digital filtering [36]. The same approach can be readily adapted to other MRI control platforms. In systems that do not provide an explicit noise-acquisition sequence, equivalent information can be extracted from a simple free-induction decay acquisition with the RF excitation amplitude set to zero.

3.2 | In Vivo Imaging Acquisitions

All in vivo images in this work were acquired with the MUST scanner described in Section 2, after the upgrades described in Section 3.1. Experiments employed three-dimensional Rapid Acquisition with Relaxation Enhancement (3D-RARE) sequences optimized for low-field operation, using a repetition time (TR) and echo spacing time (TE) suitable for either T_1- or T_2-weighted contrast. All sequence parameters are summarized in Table 1.

To investigate the most favorable subject positioning within the unshimmed 46-mT magnet, further T_1-weighted images were acquired with the head placed at different positions inside the magnet bore.

To mitigate the geometric distortions resulting from field inhomogeneity, we implemented a data processing pipeline that incorporates prior knowledge of the spatial B_0 distribution during image reconstruction. The magnetic field map was obtained using the Single-Point Double-Shot (SPDS) method [30], and the reconstructed data were processed with this field information (Conjugate Phase [46] or Algebraic Reconstruction Techniques [47]). In brief, SPDS consists of acquiring two low-resolution images using SPRITE (Single-Point Ramped Imaging with T_1 enhancement), with identical spatial encoding but slightly different dead times following the RF excitation pulse. Because SPRITE is intrinsically insensitive to geometric distortions, the phase difference between the two images provides a faithful estimate of the local B_0 field, even in the presence of strong inhomogeneities. In practice, this field map can be acquired using a large homogeneous phantom prior to the imaging sessions and subsequently used for distortion correction, provided that the field does not undergo significant temporal drift. Because these algorithms are computationally intensive, the reconstruction was executed remotely through Tyger.

4 | Results

4.1 | Scanner Revamp and Electromagnetic Noise Suppression

Before discussing the individual results in detail, it is worth summarizing three outcomes that stem from the combined hardware and software revamp described in Section 3.1. First, the upgrade of MaRCoS with the MaRGE graphical environment transformed scanner operation from a command-line-based workflow into an integrated graphical interface, providing automated calibration procedures (including Larmor frequency determination, RF transmit amplitude calibration, and gradient-based B_0 shimming), access to pre-installed families of pulse sequences (most notably RARE and SPDS in the present work) with full control over sequence parameters (e.g., TE, TR, partial Fourier acquisition, inversion preparation), and multiple built-in options for image reconstruction, visualization, and data processing. Details on all these procedures can be found in Ref. [37]. Second, remote processing significantly reduced reconstruction turnaround times by enabling computationally demanding distortion-correction and model-based reconstruction pipelines to be executed on GPU-equipped cloud

10991492, 2026, 6, Downloaded from https://analyticalsciencejournals.onlinelibrary.wiley.com/doi/10.1002/nbm.70293 by Mbarara Univ of Science and Te, Wiley Online Library on [13/05/2026]. See the Terms and Conditions (https://onlinelibrary.wiley.com/terms-and-conditions) on Wiley Online Library for rules of use; OA articles are governed by the applicable Creative Commons License

TABLE 1 | Acquisition parameters for the images included in this work.

Figure	FoV (mm3)	# pixels	Partial Fourier (%)	Resolution (mm3)	BW (kHz)	TR (ms)	TE (ms)	ETL	*k*-space filling	Avgs.	Scan time (min)
Figure 6 T1w	179 × 192 × 117	100 × 100 × 24	100	1.7 × 1.9 × 4.8	16.6	600	16	5	Center-out	7	33
Figure 6 T2w	195 × 210 × 140	80 × 80 × 18	85	2.4 × 2.6 × 7.7	13.3	2500	40	8	Linear	7	44
Figure 7	120 × 160 × 120	90 × 90 × 16	65	1.7 × 1.3 × 7.5	22.5	200	20	5	Center-out	40	24
Figure 8 top	185 × 200 × 142	100 × 100 × 24	80	1.8 × 2.0 × 5.9	16.6	600	16	5	Center-out	8	30
Figure 8 bottom	179 × 192 × 117	100 × 100 × 24	100	1.7 × 1.9 × 4.8	16.6	600	16	5	Center-out	7	33
Figure 9	209 × 208 × 152	100 × 100 × 24	85	2.1 × 2.1 × 6.3	16.6	600	16	5	Center-out	10	40

Note: All datasets were acquired using a 3D RARE sequence; TE denotes the effective echo time. Partial Fourier undersampling is applied only along the slice direction. Note that the image in Figure 8 bottom corresponds to the same dataset as Figure 6 T1w. RF pulse times are all around 250 μs for $\pi/2$-pulses.

infrastructure, reducing processing times from hours or days on the local control computer to the order of tens of seconds to a few minutes. Finally, and most critically, the systematic electromagnetic noise characterization and suppression protocol reduced the effective noise floor of the system to levels compatible with thermal noise dominance.

Regarding the latter, Figure 4b summarizes the normalized RMS noise measurements obtained under the three configurations introduced in Section 3.1. The plot follows the structure of Ref. [40], where each row corresponds to a specific hardware configuration. Values are expressed in units of the thermal limit. The first line ("LNA") corresponds to a minimal receive chain comprising only the low-noise amplifier and digitizer, with all other components physically disconnected. The subsequent rows show the progressive addition of subsystems: insertion of the TxRx switch, connection of the transmit electronics, activation of the RFPA, and activation of the GPAs.

Figure 5 shows the RMS noise level monitored continuously over a period of nearly three days. The measurement was carried out with the scanner in its revamped configuration and after proper grounding of all elements.

4.2 | In Vivo Imaging

Representative brain and knee images acquired with the upgraded system and reconstructed via Tyger are shown in Figures 6 and 7.

The influence of subject positioning on image quality is illustrated in Figure 8. The top row corresponds to a T_1-weighted acquisition with the head positioned at the geometric center of the magnet. The bottom row shows the same subject displaced downwards (closer to the room floor).

Finally, the effect of distortion correction using SPDS-based reconstruction is presented in Figure 9. The top row displays the measured B_0 field maps, the middle row shows conventional Fourier reconstructions, and the bottom row presents the corrected images.

5 | Discussion

5.1 | Scanner Revamp and Electromagnetic Noise Suppression

The noise characterization in Figure 4b provides a quantitative view of the scanner's deviation from the theoretical thermal limit. Even in the simplest configuration (LNA connected to a 50Ω load) the measured noise is about 1.9× the thermal level, indicating that the commercial LNA used in the system introduces a significant contribution. This observation connects directly to the hardware limitations discussed in Section 2: In resource-constrained settings, access to high-performance amplifiers with sub-dB noise figures is limited.

Replacing the load with the RF coil leads to a clear increase in noise, consistent with the coil's intrinsic sensitivity and the

10991492, 2026, 6, Downloaded from https://analyticalsciencejournals.onlinelibrary.wiley.com/doi/10.1002/nbm.70293 by Mbarara Univ of Science and Te, Wiley Online Library on [13/05/2026]. See the Terms and Conditions (https://onlinelibrary.wiley.com/terms-and-conditions) on Wiley Online Library for rules of use; OA articles are governed by the applicable Creative Commons License

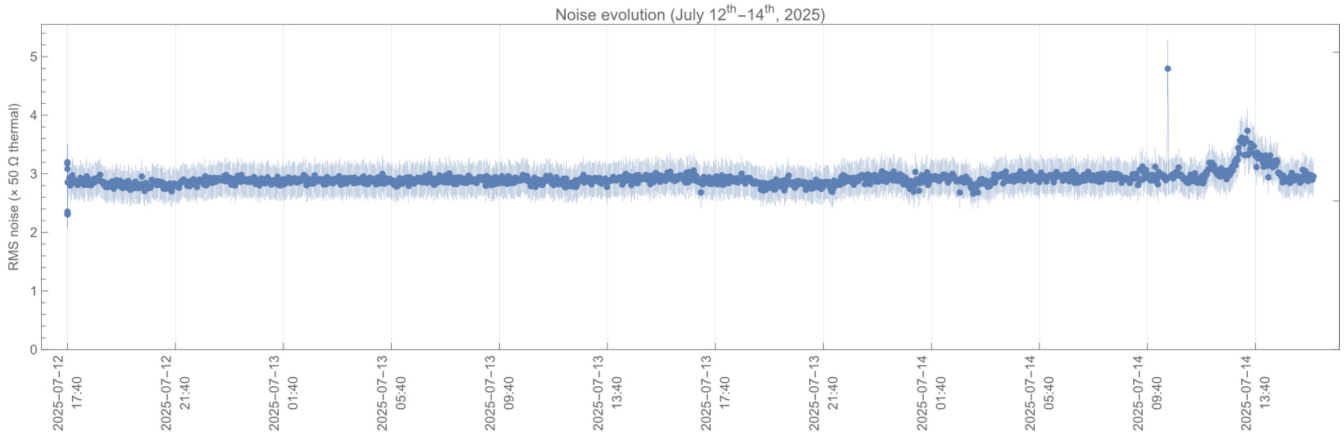


FIGURE 5 | Long-term noise monitoring with the revamped MUST scanner optimally shielded. The plot shows the evolution of the RMS noise level over a continuous period of nearly three days.

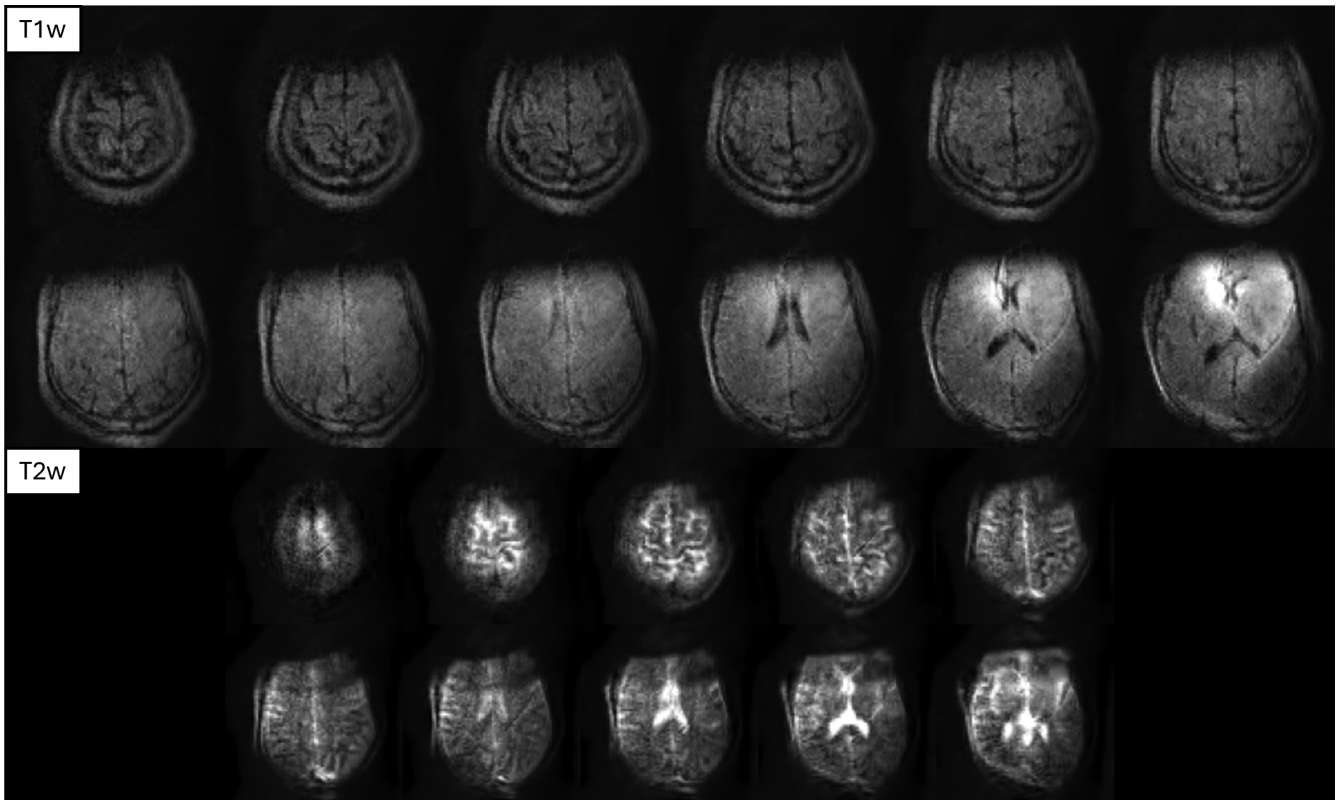


FIGURE 6 | Selected slices from two 3D brain acquisitions, a T_1-weighted image (top), and a T_2-weighted image (bottom). Both datasets were acquired using the updated hardware as described in Section 3.2. Images were acquired using the parameters listed in Table 1 and distortion-corrected via Tyger.



FIGURE 7 | Selected slices from a three-dimensional T_1w knee acquisition. Dataset acquired using the updated hardware as described in Section 3.2, with parameters in Table 1.

10991492, 2026, 6, Downloaded from https://analyticalsciencejournals.onlinelibrary.wiley.com/doi/10.1002/nbm.70293 by Mbarara Univ of Science and Te, Wiley Online Library on [13/05/2026]. See the Terms and Conditions (https://onlinelibrary.wiley.com/terms-and-conditions) on Wiley Online Library for rules of use; OA articles are governed by the applicable Creative Commons License

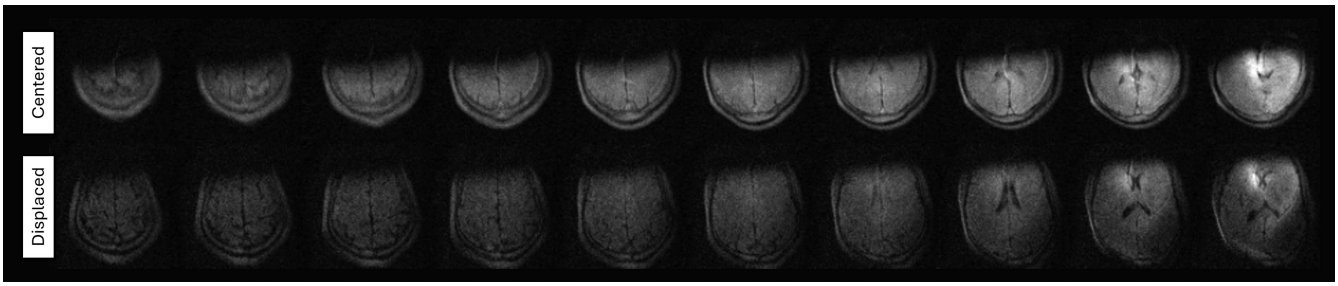


FIGURE 8 | Effect of subject positioning on brain reconstructions. Top row: the subject positioned at the geometric center of the magnet, where B_0 inhomogeneity is more pronounced. Bottom row: the same acquisition with the head displaced downwards, toward a region of improved field homogeneity. The two datasets shown were acquired using identical RF excitation and refocusing pulses and the same core sequence parameters (bandwidth, TR, TE, echo train length, and k-space filling), as detailed in Table 1 and distortion-corrected via Tyger. A slight partial Fourier undersampling was applied only for the top image to reduce acquisition time; this does not affect the observed signal non-uniformity, which is dominated by the magnetic field inhomogeneity.

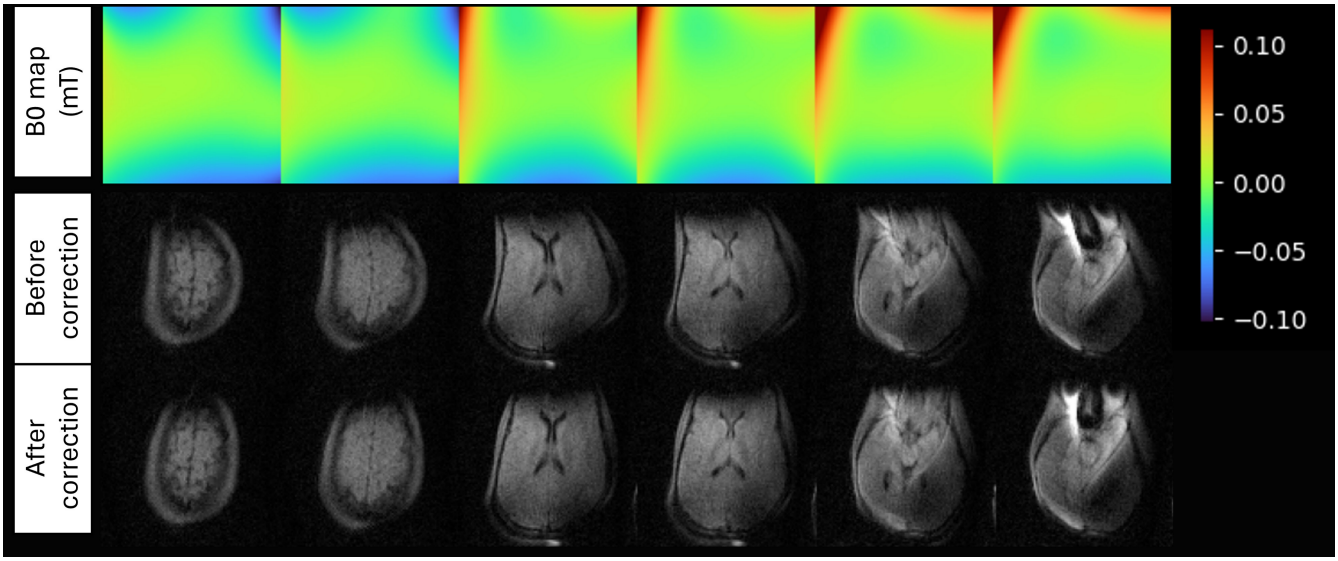


FIGURE 9 | Distortion correction using the SPDS method and cloud-based reconstruction with Tyger. Top row: measured B_0 field maps obtained with SPDS [30]. Middle row: conventional reconstruction without accounting for B_0 inhomogeneity. Bottom row: reconstruction incorporating prior knowledge of the measured field map. The correction substantially reduces geometric distortions, particularly in the frontal regions of the brain. Images were acquired using the parameters listed in Table 1 and distortion-corrected via Tyger.

coupling of external EMI. Tests performed while powering the system from an uninterruptible power supply (UPS) showed that disconnecting from the mains reduced the noise to near the 2× baseline, confirming the grid as a major noise source. However, the available UPS provided an autonomy of only ~2 min, precluding continuous battery-powered operation. The highest level (5.1×) was observed when the coil and LNA were connected without proper grounding. This is even higher than for the in vivo measurement and reflects the strong noise fluctuations in the system when grounding is unreliable. As additional grounded elements were incorporated into the setup, the system became progressively more stable. Importantly, except in situation I (minimal Rx chain), noise level changes were found to be fully reproducible across repeated measurements and acquisition sessions, indicating that they are intrinsic to the system configuration rather than a consequence of transient or unstable ambient noise.

The long-term noise measurement in Figure 5 confirms a substantial improvement in electromagnetic stability (with respect to Figure 2a) after the complete scanner revamp. Over nearly three days of continuous monitoring, the noise remained close to the achieved floor with minimal drift. Although much of this measurement was acquired during a weekend, the results indicate that the revised grounding and shielding layout effectively mitigated the intermittent noise fluctuations previously observed. In practice, the largest improvements originated from two specific changes: (i) establishing a single, low-impedance ground reference for all subsystems and (ii) enclosing the analog electronics in continuous, well-bonded conductive housings. The first step eliminated floating reference potentials and reduced common-mode pickup, which had previously led to large fluctuations in the measured noise floor. The second minimized radiative coupling into the receive chain, particularly from nearby digital electronics and the power grid. These modifications explain the marked reduction in intermittent noise excursions seen after the revamp. Noise factors below 3× can now be routinely achieved during in vivo operation. Although not ideal, this level suffices for quality data acquisition. The brief increase in noise observed around 13:30 on July 14, and a small outlier

10991492, 2026, 6, Downloaded from https://analyticalsciencejournals.onlinelibrary.wiley.com/doi/10.1002/nbm.70293 by Mbarara Univ of Science and Te, Wiley Online Library on [13/05/2026]. See the Terms and Conditions (https://onlinelibrary.wiley.com/terms-and-conditions) on Wiley Online Library for rules of use; OA articles are governed by the applicable Creative Commons License

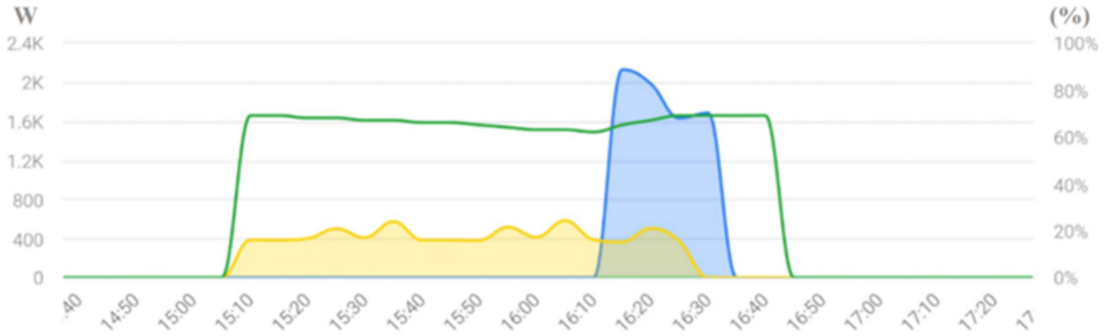


FIGURE 10 | Power consumption and battery state during operation of the 90-mT NextMRI scanner powered by a BLUETTI AC300 + 2xB300K system. Yellow: instantaneous power drawn by the scanner. Blue: battery charging state. Green: battery charge level.

earlier that same day, are both minor compared with the large fluctuations seen before the upgrade.

All in all, the systematic application of the grounding and shielding guidelines in Ref. [40] was critical to achieving stable operation closer to the thermal noise limit.

5.2 | In Vivo Imaging

The in vivo brain images presented in Figure 6 represent a significant milestone for the MUST scanner and a clear step forward from the preliminary results of 2023 (Figure 1b). While the images are not yet free from imperfections, the leap in performance is evident: Anatomical structures are now discernible, the achieved spatial resolution is adequate for low-field operation, and two fundamental contrasts (T_1- and T_2-weighting) have been successfully demonstrated. These results confirm that the revamped setup, together with the implemented noise suppression strategies and improved control electronics, provides sufficient stability and sensitivity for reliable in vivo imaging.

Signal nonuniformity remains visible, particularly in the upper portions of the images, which correspond to the frontal regions of the head. This darkening arises primarily from the limited output power of the 1-W RF amplifier, which forced the use of relatively long pulses (around 500 μs, corresponding to an excitation bandwidth in the order of 2 kHz). At this level of B_0 inhomogeneity (about 4700 ppm at 46 mT, corresponding to a spectral spread of approximately 9 kHz), the available B_1 field would need to be $\gtrsim 5\times$ higher ($25\times$ higher power) to excite or refocus the full frequency range present in the unshimmed magnet, so only part of the head is effectively excited. The effect becomes more pronounced when the subject is positioned at the geometric center of the magnet, where B_0 is more inhomogeneous (Figure 8). This can be alleviated by shifting the head slightly downward, toward regions of improved field uniformity. This problem did not occur for knee imaging, due to the smaller size of the RF coil employed.

Magnetic field inhomogeneity remains the main factor limiting image fidelity. Conventional Fourier reconstruction methods are unable to compensate for the geometric distortions introduced by such strong B_0 variations. However, reconstructions that incorporate prior knowledge of the measured field distribution, as obtained with the SPDS mapping method [30], substantially improve the resulting images (Figure 9). Although not eliminating distortions entirely, this approach restores anatomical proportions in the most affected regions, particularly at the periphery. It should be noted, however, that no reconstruction method can recover signal in regions that were not effectively excited in the first place. Because these algorithms are computationally intensive, their integration with Tyger for cloud-based GPU execution enables practical deployment even when local computational resources are limited. The ability to stream reconstructed data back to the console in near real time through MaRGE provides an effective workflow for low-cost systems in low-resource environments. In practical terms, the raw datasets acquired in this work never exceed 32 MB, which allows them to be streamed to the cloud in approximately 1 min over a standard 3G mobile network, and within a few seconds when using WiFi or 4G connectivity. With the GPU available for this work, images were reconstructed in around half a minute [45].

Overall, these results demonstrate that, through careful hardware optimization, electromagnetic noise control, and advanced reconstruction pipelines, in vivo imaging is technically achievable on a scanner built and operated in Africa. Although the acquisitions presented here required relatively long scan times, this limitation arises primarily from the elevated noise level of the receive chain, approximately three times the Johnson noise limit. Under ideal conditions, with a lower-noise amplifier and complete isolation from grid interference, comparable image quality could in principle be achieved in roughly one-ninth of the current acquisition time. Additionally, the use of Tyger allows for advanced denoising techniques running on cloud GPUs [48]. In any case, no special measures were required to stabilize the system during acquisition beyond instructing volunteers to remain as still as possible and informing them in advance about the relatively long scan times, with subject motion being the dominant practical limitation; in contrast, temperature drifts occur on significantly longer time scales than individual acquisitions, and mechanical vibrations were not observed to be a limiting factor.

6 | Conclusions and Outlook

We have presented the first in vivo images acquired with a low-cost MRI scanner built in Africa. This work highlights both the

10991492, 2026, 6, Downloaded from https://analyticalsciencejournals.onlinelibrary.wiley.com/doi/10.1002/nbm.70293 by Mbarara Univ of Science and Tec, Wiley Online Library on [13/05/2026]. See the Terms and Conditions (https://onlinelibrary.wiley.com/terms-and-conditions) on Wiley Online Library for rules of use; OA articles are governed by the applicable Creative Commons License

technological feasibility and the capacity-building aspects of deploying affordable MRI systems in low-resource settings, paving the way toward clinical translation.

From a technical standpoint, scanner performance is still largely constrained by electromagnetic noise and the instability of power grids in low-resource environments. Recent work with battery-powered systems demonstrates that autonomous operation can overcome many of these limitations. Using a commercial system (BLUETTI AC300 + 2xB300K) as the sole power source for a 90-mT NextMRI scanner [49], stable operation was achieved with power consumption below 600 W during scanning and approximately 400 W when idle (Figure 10). This configuration provides about 9 h of continuous MRI operation and allows hot-swappable, seamless recharging while isolating the scanner from mains noise. Extending this approach to autonomous low-field scanners could be relevant to achieving consistent image quality and reliable operation in low-resource settings.

In addition to electromagnetic noise, the other major limitation that currently constrains image quality is the intrinsic B_0 inhomogeneity of permanent-magnet Halbach arrays. Distortions arising from inhomogeneities spanning several kHz ultimately limit excitation coverage. While recent open-source initiatives have begun to make field-mapping hardware more accessible, for example, low-cost robotic arms for characterizing Halbach fields [50], the practical implementation of passive shimming remains challenging. There is currently no simple, robust, and broadly accessible methodology for shimming permanent-magnet arrays. Existing strategies typically rely on intricate optimization procedures, custom simulation workflows, or highly-precise inserts that are difficult to design and validate even in well-equipped laboratories. Developing a straightforward, replicable shimming approach suitable for both research and low-resource environments therefore remains an important open challenge for the wider low-field MRI community.

Despite the progress demonstrated here, a number of challenges remain before low-cost MRI can reach widespread and sustainable use in SSA. Capacity building continues to be a major bottleneck, both from the user and clinical perspective and from the technical and industrial side. Low-field MRI technologies are beginning to mature globally, yet local expertise in SSA remains limited, hindering system maintenance, operation, and eventual clinical translation. Developing regional training programs and fostering industrial partnerships will be essential to ensure that locally deployed systems can be effectively utilized and supported [5]. Although pilot clinical studies are under way worldwide, translation to routine healthcare remains slow and will require regulatory frameworks and reliable maintenance pathways that are still in their infancy in low- and middle-income countries. For a more detailed discussion, we refer to Ref. [18].

Author Contributions

Scanner revamp by T.G-N., R.As., P.T., M.A.N., L.K., L.R., M.N., L.G.C.S., L.S., J.M.A., R.Am., and J.A. Data acquisition by T.G-N., R.As., P.T., M.A.N., R.Am., and J.A. MaRGE coding by T.G-N. and J.M.A. Tyger development by J.S. and M.H. Tyger integration by T.G-N. and J.M.A. Battery tests by T.G-N., R.As., P.T., M.A.N., L.G.C.S., J.M.A., and J.A. Project conceived by T.G-N., A.W., J.H., S.J.S., J.O., and J.A. Project managed by M.F.G., R.Am., A.W., J.H., S.J.S., J.O., and J.A. Figure production by T.G-N., L.K., and J.A. Paper written by T.G-N. and J.A., with input from all authors.

Acknowledgments

We thank Tom O'Reilly for contributing to the first stages of the scanner revamp and for participating in the conception of the project and Danny de Gans for assistance restoring the functionality of the GPA.

Funding

This work was supported by Ministerio de Ciencia e Innovación (PID2022-142719OB-C22), the European Innovation Council (NextMRI 101136407), the ISMRM-Gates Knowledge Exchange Program (91484), and US NIH grant 5R01HD085853-1.

Conflicts of Interest

T.G-N. consults for PhysioMRI Tech. J.M.A. and J.A. are co-founders of PhysioMRI Tech.

Data Availability Statement

The data that support the findings of this study are available from the corresponding author upon reasonable request.

Endnotes

[1] The OSII open repository [39] contains RF coil designs similar to those employed in this work.

[2] We did not yet install an automatic impedance tuning and matching box [42] due to lack of components.

[3] Technical details on the integration between Tyger and MaRGE can be found in a separate work [45].

References

1. S. Murali, H. Ding, F. Adedeji, et al., "Bringing MRI to Low-and Middle-Income Countries: Directions, Challenges and Potential Solutions," *NMR in Biomedicine* 37, no. 7 (2024): e4992.

2. S. Geethanath and J. T. Vaughan, Jr., "Accessible Magnetic Resonance Imaging: A Review," *Journal of Magnetic Resonance Imaging* 49, no. 7 (2019): e65–e77.

3. H. Hricak, M. Abdel-Wahab, R. Atun, et al., "Medical Imaging and Nuclear Medicine: A Lancet Oncology Commission," *Lancet Oncology* 22 (2021): e136–e172.

4. "Sub-Saharan Africa - Total Population 2013–2023 — Statista," https://www.statista.com/statistics/805605/total-population-sub-saharan-africa/.

5. U. C. Anazodo, J. J. Ng, B. Ehiogu, et al., "A Framework for Advancing Sustainable Magnetic Resonance Imaging Access in Africa," *NMR in Biomedicine* 36, no. 3 (2023): e4846.

6. M. C. Dewan, A. Rattani, R. Mekary, et al., "Global Hydrocephalus Epidemiology and Incidence: Systematic Review and Meta-Analysis," *Journal of Neurosurgery* 130 (2018): 1065–1079, https://thejns.org/view/journals/j-neurosurg/130/4/article-p1065.xml.

7. J. R. Harper, V. Cherukuri, T. O'Reilly, et al., "Assessing the Utility of Low Resolution Brain Imaging: Treatment of Infant Hydrocephalus," *NeuroImage: Clinical* 32 (2021): 102896.

8. S. S. Bhat, T. T. Fernandes, P. Poojar, et al., "Low-Field MRI of Stroke: Challenges and Opportunities," *Journal of Magnetic Resonance Imaging* 54, no. 2 (2021): 372–390, https://doi.org/10.1002/jmri.27324.

10991492, 2026, 6, Downloaded from https://analyticalsciencejournals.onlinelibrary.wiley.com/doi/10.1002/nbm.70293 by Mbarara Univ of Science and Te, Wiley Online Library on [13/05/2026]. See the Terms and Conditions (https://onlinelibrary.wiley.com/terms-and-conditions) on Wiley Online Library for rules of use; OA articles are governed by the applicable Creative Commons License

9. L. Carnis, D. Mignot, "Road Safety Management in Africa: Challenges and Solutions for Tomorrow," in XXVII World Road Congress Prague 2023, 2023, 1.

10. "Road Safety Week: African Nations Steer Towards Reducing Deaths—UN News," https://news.un.org/en/story/2023/05/1136627.

11. Y. Kumar and D. Hayashi, "Role of Magnetic Resonance Imaging in Acute Spinal Trauma: A Pictorial Review," *BMC Musculoskeletal Disorders* 17 (2016): 1–11.

12. A. L. Deutsch and J. H. Mink, "Magnetic Resonance Imaging of Musculoskeletal Injuries," *Radiologic Clinics of North America* 27 (1989): 983–1002.

13. G. D. Deyle, "The Role of MRI in Musculoskeletal Practice: A Clinical Perspective," *Journal of Manual & Manipulative Therapy* 19 (2011): 152–161, https://doi.org/10.1179/2042618611Y.0000000009.

14. M. Sarracanie, C. D. LaPierre, N. Salameh, D. E. J. Waddington, T. Witzel, and M. S. Rosen, "Low-Cost High-Performance MRI," *Scientific Reports* 5, no. 1 (2015): 15177 http://www.nature.com/articles/srep15177.

15. J. P. Marques, F. F. Simonis, and A. G. Webb, "Low-Field MRI: An MR Physics Perspective," *Journal of Magnetic Resonance Imaging* 49, no. 6 (2019): 1528–1542, https://doi.org/10.1002/jmri.26637.

16. M. Sarracanie and N. Salameh, "Low-Field MRI: How Low Can We Go? A Fresh View on an Old Debate," *Frontiers in Physics* 8 (2020): 172, https://doi.org/10.3389/fphy.2020.00172/full.

17. L. L. Wald, P. C. McDaniel, T. Witzel, J. P. Stockmann, and C. Z. Cooley, "Low-Cost and Portable MRI," *Journal of Magnetic Resonance Imaging* 52, no. 3 (2020): 686–696, https://doi.org/10.1002/jmri.26942.

18. A. Webb and J. Obungoloch, "Five Steps to Make MRI Scanners More Affordable to the World," *Nature* 615 (2023): 391–393, https://www.nature.com/articles/d41586-023-00759-x.

19. P. C. McDaniel, C. Z. Cooley, J. P. Stockmann, and L. L. Wald, "The MR Cap: A Single-Sided MRI System Designed for Potential Point-of-Care Limited Field-of-View Brain Imaging," *Magnetic Resonance in Medicine* 82, no. 5 (2019): 1946–1960, https://doi.org/10.1002/mrm.27861.

20. M. Nakagomi, M. Kajiwara, J. Matsuzaki, et al., "Development of a Small Car-Mounted Magnetic Resonance Imaging System for Human Elbows Using a 0.2 T Permanent Magnet," *Journal of Magnetic Resonance* 304 (2019): 1–6.

21. C. Z. Cooley, P. C. McDaniel, J. P. Stockmann, et al., "A Portable Scanner for Magnetic Resonance Imaging of the Brain," *Nature Biomedical Engineering* 5, no. 3 (2020): 229–239, https://www.nature.com/articles/s41551-020-00641-5.

22. T. O'Reilly, W. M. Teeuwisse, D. Gans, K. Koolstra, and A. G. Webb, "In Vivo 3D Brain and Extremity MRI at 50 mT Using a Permanent Magnet Halbach Array," *Magnetic Resonance in Medicine* mrm.28396 (2020): 495–505, https://doi.org/10.1002/mrm.28396.

23. K. N. Sheth, M. H. Mazurek, M. M. Yuen, et al., "Assessment of Brain Injury Using Portable, Low-Field Magnetic Resonance Imaging at the Bedside of Critically Ill Patients," *JAMA Neurology* 78, no. 1 (2021): 41–47, https://jamanetwork.com/journals/jamaneurology/fullarticle/2769858.

24. M. H. Mazurek, M. M. Yuen, B. A. Cahn, et al., "Low-Field, Portable Magnetic Resonance Imaging at the Bedside to Assess Brain Injury in Patients With Severe COVID-19 (1349)," *Neurology* 96, no. 15 Supplement (2021): 1349.

25. Y. Liu, A. T. L. Leong, Y. Zhao, et al., "A Low-Cost and Shielding-Free Ultra-Low-Field Brain MRI Scanner," *Nature Communications* 12, no. 1 (2021): 1–14, https://www.nature.com/articles/s41467-021-27317-1.

26. T. Guallart-Naval, J. M. Algarín, R. Pellicer-Guridi, et al., "Portable Magnetic Resonance Imaging of Patients Indoors, Outdoors and at Home," *Scientific Reports* 12, no. 1 (2022): 1–11, https://www.nature.com/articles/s41598-022-17472-w.

27. T. O'Reilly and A. G. Webb, "In Vivo T1 and T2 Relaxation Time Maps of Brain Tissue, Skeletal Muscle, and Lipid Measured in Healthy Volunteers at 50 mT," *Magnetic Resonance in Medicine* 87, no. 2 (2021): 884–895, https://doi.org/10.1002/mrm.29009.

28. M. Sarracanie, "Fast Quantitative Low-Field Magnetic Resonance Imaging With OPTIMUM - Optimized Magnetic Resonance Fingerprinting Using a Stationary Steady-State Cartesian Approach and Accelerated Acquisition Schedules," *Investigative Radiology* 57, no. 4 (2022): 263–271, https://journals.lww.com/investigativeradiology/Fulltext/9000/Fast_Quantitative_Low_Field_Magnetic_Resonance.98659.aspx.

29. J. M. Algarín, E. Díaz-Caballero, J. Borreguero, et al., "Simultaneous Imaging of Hard and Soft Biological Tissues in a Low-Field Dental MRI Scanner," *Scientific Reports* 10, no. 1 (2020): 21470, https://doi.org/10.1038/s41598-020-78456-2.

30. J. Borreguero, F. Galve, J. M. Algarín, and J. Alonso, "Zero-Echo-Time Sequences in Highly Inhomogeneous Fields," *Magnetic Resonance in Medicine* 93, no. 3 (2025): 1190–1204, https://doi.org/10.1002/mrm.30352.

31. J. Borreguero, L. G. C. Santos, L. V. Cid, et al., "Qualitative and Quantitative Hard-Tissue MRI With Portable Halbach Scanners," arXiv preprint arXiv:2511.15617, 2025, https://arxiv.org/abs/2511.15617.

32. C. D. Van Speybroeck, T. O'Reilly, W. Teeuwisse, P. M. Arnold, and A. G. Webb, "Characterization of Displacement Forces and Image Artifacts in the Presence of Passive Medical Implants in Low-Field," *Physica Medica* 84 (2021): 116–124, https://pubmed.ncbi.nlm.nih.gov/33894581/.

33. Y. Qiu, K. Dai, S. Zhong, et al., "Spatiotemporal Encoding MRI in a Portable Low-Field System," *Magnetic Resonance in Medicine* 92, no. 3 (2024): 1011–1021.

34. Y. Zhao, Y. Ding, V. Lau, et al., "Whole-Body Magnetic Resonance Imaging at 0.05 Tesla," *Science* 384 (2024): 5, https://doi.org/10.1126/science.adm7168.

35. J. Obungoloch, I. Muhumuza, W. Teeuwisse, et al., "On-Site Construction of a Point-of-Care Low-Field MRI System in Africa," *NMR in Biomedicine* 36, no. 7 (2023): e4917.

36. V. Negnevitsky, Y. Vives-Gilabert, J. M. Algarín, et al., "MaRCoS, an Open-Source Electronic Control System for Low-Field MRI," *Journal of Magnetic Resonance* 350 (2023): 107424, https://doi.org/10.1016/j.jmr.2023.107424.

37. J. M. Algarín, T. Guallart-Naval, J. Borreguero, F. Galve, and J. Alonso, "MaRGE: A Graphical Environment for MaRCoS," *Journal of Magnetic Resonance* 361 (2024): 107662.

38. "Github—Microsoft/Tyger: Remote Signal Processing," https://github.com/microsoft/tyger.

39. "Gitlab—OSII," https://gitlab.com/osii.

40. T. Guallart-Naval, J. M. Algarín, and J. Alonso, "Electromagnetic Noise Characterization and Suppression in Low-Field MRI Systems," *Magnetic Resonance in Medicine* 95, no. 5 (2026): 3000–3007, https://doi.org/10.1002/mrm.70235.

41. T. O'Reilly, W. Teeuwisse, and A. Webb, "A New Approach to Shimming Halbach Arrays Using Higher Order Halbach Array Inserts," in *Proceedings of the 2022 ISMRM Annual Meeting and Exhibition in Paris* (ISMRM, 2022), 63.

42. "GitHub—RFAutoMaTE," https://github.com/josalggui/RFAutoMaTE.

43. "GitHub—MaRCoS MRI," https://github.com/marcos-mri.

44. "GitHub—MaRGE," https://github.com/marcos-mri/MaRGE.

10991492, 2026, 6, Downloaded from https://analyticalsciencejournals.onlinelibrary.wiley.com/doi/10.1002/nbm.70293 by Mbarara Univ of Science and Te, Wiley Online Library on [13/05/2026]. See the Terms and Conditions (https://onlinelibrary.wiley.com/terms-and-conditions) on Wiley Online Library for rules of use; OA articles are governed by the applicable Creative Commons License

45. T. Guallart-Naval, J. Stairs, J. M. Algarín, et al., "A Fully Open-Source Framework for Streaming and Cloud-Processing of Low-Field MRI Data," arXiv preprint arXiv: 2603.19287, 2026, https://arxiv.org/abs/2603.19287.

46. A. Macovski, "Volumetric NMR Imaging With Time-Varying Gradients," *Magnetic Resonance in Medicine* 2, no. 1 (1985): 29–40.

47. S. Karczmarz, "Angenäherte Auflösung von Systemen Linearer Gleichungen," *Bulletin International de l'Académie Polonaise des Sciences et des Lettres, Classe des Sciences Mathématiques et Naturelles* 35 (1937): 355–357.

48. H. Xue, S. M. Hooper, I. Pierce, et al., "SNRAware: Improved Deep Learning MRI Denoising With Signal-to-Noise Ratio Unit Training and g-Factor Map Augmentation, Radiology," *Artificial Intelligence* 7, no. 6 (2025): e250227, https://doi.org/10.1148/ryai.250227.

49. F. Galve, E. Pallás, T. Guallart-Naval, et al., "Elliptical Halbach Magnet and Gradient Modules for Low-Field Portable Magnetic Resonance Imaging," *NMR in Biomedicine* 37, no. 12 (2024): e5258, https://doi.org/10.1002/nbm.5258.

50. H. Han, R. Moritz, E. Oberacker, H. Waiczies, T. Niendorf, and L. Winter, "Open Source 3D Multipurpose Measurement System With Submillimetre Fidelity and First Application in Magnetic Resonance," *Scientific Reports* 7 (2017): 13452.

10991492, 2026, 6, Downloaded from https://analyticalsciencejournals.onlinelibrary.wiley.com/doi/10.1002/nbm.70293 by Mbarara Univ of Science and Te, Wiley Online Library on [13/05/2026]. See the Terms and Conditions (https://onlinelibrary.wiley.com/terms-and-conditions) on Wiley Online Library for rules of use; OA articles are governed by the applicable Creative Commons License